Geophysical Research Letters

RESEARCH LETTER
10.1029/2022GL098626

Key Points:

- On 15 January 2022, a wide variety of gravity wave scales were excited by the eruption of the Hunga Tonga-Hunga Ha'apai volcano
- We here focus on characterizing and quantifying the mesoscale response and confirm by backtracing the eruption as source of these waves
- Compared to usual conditions amplitudes and momentum flux of the eruption wave event are strong for Microwave Limb Sounder and exceptional for Atmospheric Infrared Sounder

Correspondence to:
M. Ern,
m.ern@fz-juelich.de

Citation:
Ern, M., Hoffmann, L., Rhode, S., & Preusse, P. (2022). The mesoscale gravity wave response to the 2022 Tonga volcanic eruption: AIRS and MLS satellite observations and source backtracing. *Geophysical Research Letters*, *49*, e2022GL098626. https://doi.org/10.1029/2022GL098626

Received 8 MAR 2022
Accepted 11 MAY 2022

The Mesoscale Gravity Wave Response to the 2022 Tonga Volcanic Eruption: AIRS and MLS Satellite Observations and Source Backtracing

M. Ern[1], L. Hoffmann[2], S. Rhode[1], and P. Preusse[1]

[1]Institut für Energie- und Klimaforschung (IEK-7), Forschungszentrum Jülich GmbH, Jülich, Germany, [2]Jülich Supercomputing Centre, Forschungszentrum Jülich GmbH, Jülich, Germany

Abstract On 15 January 2022, the Hunga Tonga–Hunga Ha'apai volcano erupted violently. This exceptional event excited a manifold of atmospheric waves. Here, we focus on the mesoscale part of the wave spectrum. About 8.5 hr after the eruption a strong atmospheric gravity wave (GW) was observed in the stratosphere by the satellite instruments Atmospheric Infrared Sounder (AIRS) and Microwave Limb Sounder (MLS) in the vicinity of Tonga. By ray-tracing, we confirm the eruption as the source of this GW event. We determine the wave characteristics of the GW in terms of horizontal and vertical wavelengths and GW momentum flux. The strength of the GW is compared to the usual Southern Hemisphere flux values during this week. The event is comparable to the strongest convective events considering MLS, and exceptionally strong considering AIRS, which observes faster waves only.

Plain Language Summary Atmospheric gravity waves (GWs) are small- and mesoscale waves typically generated by convective events, jet instabilities, or flow over orography. On 15 January 2022, an explosive eruption of the Hunga Tonga–Hunga Ha'apai volcano occurred. This eruption was a source of strong GWs of a wide range of wavelengths and phase speeds. We here focus on mesoscale waves and in particular on vertical wavelengths with the potential for interaction with the background wind, that is, vertical scales usually considered for driving atmospheric circulation. Observations by two different types of satellite instruments (limb sounding and nadir sounding) give us the unique opportunity for a detailed study of this GW event originating from a source process that has rarely been considered so far. Tracing the wave backward in time using a wave-propagation model confirms the volcanic eruption as the wave source. Horizontal and vertical wavelengths of the GW are 500 and 20 km, respectively. Amplitudes and momentum flux indicate that the event is outstanding in particular for the higher phase speeds. We consider this rare wave event highly interesting for future more detailed observational studies, as well as for atmospheric modeling.

1. Introduction

Atmospheric gravity waves (GWs) are usually excited by processes such as flow over orography (e.g., Eckermann & Preusse, 1999; Hoffmann et al., 2013; Jiang et al., 2004; Kruse et al., 2022), spontaneous imbalance (e.g., Plougonven & Zhang, 2014, and references therein), and convection (e.g., Alexander et al., 1995; Beres et al., 2005; Chun & Baik, 1998; Trinh et al., 2016). Only rarely, volcanic eruptions were discussed as a potential source (e.g., Gossard & Hooke, 1975; Yue et al., 2022). On 15 January 2022, at 04:14:45 UTC a violent eruption of the Hunga Tonga–Hunga Ha'apai volcano (20.536°S, 175.382°W) started (Global Volcanism Program, 2022; USGS Earthquakes Hazards Program, 2022), likely being the world's largest eruption for decades (Poli & Shapiro, 2022; Radio New Zealand, 2022; Wright et al., 2022). One spectacular middle atmosphere response to the Tonga eruption were very fast GWs of around 250 m/s phase speed (Wright et al., 2022). Being much faster than the background wind, these GWs were not wind-modulated and formed almost ideally circular quasi-concentric wave patterns extending several thousand kilometers in diameter (Adam, 2022; Wright et al., 2022). These phase speeds are far beyond typical phase speeds where source momentum fluxes of GW parameterizations for the middle atmosphere are peaking (several tens m/s, corresponding to vertical wavelengths <approximately 20 km, e.g., Alexander & Dunkerton, 1999; Beres et al., 2005; Trinh et al., 2016).

Here, we focus on the phase speed range <100 m/s that is believed to be responsible for the driving of, for example, the mesospheric circulation (e.g., Holton, 1983), or the quasi-biennial oscillation (QBO) and semi-annual oscillation (SAO) in the tropics (e.g., Baldwin et al., 2001; Ern et al., 2014, 2015, 2021; Hamilton &

Mahlman, 1988; Lindzen & Holton, 1968). We investigate the mesoscale GWs excited by the eruption using observations from the Atmospheric Infrared Sounder (AIRS) and Microwave Limb Sounder (MLS) satellite instruments. We determine GW temperature amplitudes, as well as horizontal and vertical wavelengths, and confirm the wave source by GW backward ray tracing. Further, we determine GW momentum fluxes (GWMF) to find out whether this event significantly exceeded the usual background GW activity in this region, and whether it therefore could have a stronger impact on the global circulation.

2. Description of Data Sets

2.1. The AIRS Data Set

The AIRS instrument (Aumann et al., 2003; Chahine et al., 2006) is a nadir-viewing hyperspectral infrared sounder. It was launched in May 2002 on the National Aeronautics and Space Administration (NASA) satellite Aqua. AIRS is permanently performing scans across the satellite track. One across-track scan consists of 90 individual footprints, forming a 1,780 km wide swath centered around the satellite track. (The number of 1,780 km refers to footprints at the Earth's surface.) The along-track sampling distance is 18 km. At nadir, the diameter of a footprint is 13.5 km, and the across-track sampling step is 13 km, both increasing for the off-nadir soundings. Equator crossing times of Aqua are 13:30 local solar time (LST) for ascending orbits, and 01:30 LST for descending orbits. For more details see, for example, Aumann et al. (2003), Chahine et al. (2006), or Hoffmann et al. (2014).

We utilize temperatures retrieved from AIRS radiance observations. The retrieval method is described in detail in Hoffmann and Alexander (2009). Here, we focus on descending AIRS orbits only, which means nighttime data in the region of our interest. During nighttime, AIRS observations of the atmospheric CO_2 emission bands at 4.3 and 15 μm can be combined, resulting in improved altitude resolution and reduced noise. The Hoffmann and Alexander (2009) retrieval approach is optimized for the analysis of GWs by utilizing the single-footprint horizontal resolution of AIRS. This is different from the operational retrieval which combines blocks of 3×3 footprints (Cho & Staelin, 2006; Susskind et al., 2003). Further, the retrieval of Hoffmann and Alexander (2009) represents a tradeoff between retrieval noise and vertical resolution. The vertical retrieval step is 3 km at altitudes below 60 km, while the effective vertical resolution is coarser and varies between 7 km at 20 km altitude and 15 km at 60 km altitude. This vertical resolution is improved with respect to the AIRS operational retrieval (Hoffmann & Alexander, 2009). Further, by combining different spectral channels, the vertical resolution of the Hoffmann and Alexander (2009) retrieval is also improved with respect to the vertical weighting functions that apply for radiances. The effect of radiance vertical weighting functions is discussed, for example, in Gong et al. (2012). According to the vertical resolution mentioned above, our AIRS temperatures are sensitive to GWs of vertical wavelengths $\lambda_z > 15$ km, and horizontal wavelengths λ_h of approximately 30 km to approximately 1,300 km. The 1,300 km limit comes from the background removal by an across-track fourth-order polynomial fit (Hoffmann et al., 2014). For more discussion on the AIRS observational filter see, for example, Hoffmann et al. (2014), Ern et al. (2017), or Meyer et al. (2018).

2.2. The MLS Data Set

The MLS instrument was launched on NASA's Aura satellite on 15 July 2004 into a sun-synchronous orbit with equator crossing times of 01:45 LST (descending orbits) and 13:45 LST (ascending orbits). Like Aqua, Aura is part of NASA's A-train constellation of satellites. The A-train satellites orbit the Earth one behind the other on the same track. MLS is a radiometer that observes atmospheric microwave emissions in limb-viewing geometry (Livesey et al., 2022; Waters et al., 2006). From these observations, temperature-pressure profiles and numerous trace species are derived (e.g., Livesey et al., 2022; M. J. Schwartz, 2008). We use MLS version 5.01 atmospheric temperatures and geopotential height, which are available from the middle troposphere up to the mesopause. The vertical resolution is between 3 and 4 km at pressures >10 hPa (altitudes <approximately 32 km), gradually degrading to approximately 8 km at 65 km, and to around 12 km at the mesopause (Livesey et al., 2022). Accordingly, at altitudes below 65 km MLS is sensitive to GWs of $\lambda_z > 7$–16 km, that is, MLS can observe also GWs of somewhat shorter λ_z than AIRS. However, MLS observations form only a single measurement track. Because MLS observes in limb geometry, MLS is sensitive to GWs of $\lambda_h > 100$–200 km (e.g., Alexander et al., 2010; Ern et al., 2018; Preusse et al., 2002; Preusse et al., 2008), which is worse than for AIRS. Because MLS uses

a forward-looking geometry, this partly compensates the time lag between the Aqua and Aura satellite equator crossing times, such that AIRS and MLS observations are almost coincident in time and space. Coincidence in time is better than approximately 10 min, which is much shorter than the ground-based period of approximately 4 hr of the wave event considered here. The method for determining fluctuations due to GWs from MLS temperatures is described in Appendix A.

3. AIRS and MLS Observations of the Wave Event

3.1. Temperature Fluctuations

In a first step, we investigate AIRS temperature residuals of the descending orbits on 15 January 2022 at an altitude of 36 km in the vicinity of the Tonga event (Figure 1a). Obviously, there is a prominent GW event between 30° and 10°S, east of the date line. Localized sources emit GWs with concentric circular phase fronts around the source at the center. These GWs are often modulated by the background winds (e.g., Lane et al., 2001), and only segments of the circle remain visible as a result of wind filtering, or as an effect of the instrument observational filter (e.g., Gong et al., 2015; Yue et al., 2014). The prominent curved wave fronts of the 15 January wave event are part of a circular wave pattern of this kind, and therefore indicate a localized GW source. Since the eruption of the Hunga Tonga–Hunga Ha'apai volcano occurred on this day, and since the location of the volcano (marked in Figure 1a by a magenta triangle) is close to the central point of the wave pattern, the volcanic eruption is a very likely candidate for the wave source. This will be investigated in more detail by GW backward ray tracing in Section 4.

Also marked in Figure 1a are the positions of individual MLS soundings (black diamonds) along the MLS measurement track, and the AIRS track that coincides best with the MLS observations (black line). Overpass times for the main event are about 12:50 UTC for both AIRS and MLS, that is, about 8.5 hr after the eruption. Figures 1b and 1c show latitude-altitude cross sections of AIRS and MLS temperature fluctuations obtained in the respective measurement tracks marked in Figure 1a. For AIRS, to reduce noise, we average over the best-coincidence track and its two direct neighbors in across-track direction. As can be seen from Figures 1b and 1c, the wave event appears as a V-shaped pattern in the temperature fluctuations of both AIRS and MLS. V-shaped wave patterns are another indication of a localized GW source (e.g., Alexander et al., 1995; Piani et al., 2000). Because AIRS and MLS observations are almost exactly coincident, not only in space, but also in time, the patterns match very well. Minor differences can be attributed to differences of the observational filters of the two instruments. In particular, the minimum in AIRS residual temperatures at 40 km/22°S is deeper than for MLS. Possible reasons could be observational filter variations with altitude, or short λ_z GWs that are superimposed on the V-shaped structure and are seen by MLS, but not by AIRS.

3.2. Estimation of Wave Parameters and of GWMF

3.2.1. AIRS Observations

Next, we determine the wave parameters of this prominent wave event. For AIRS, we utilize the S3D GW analysis method that was introduced by Lehmann et al. (2012) and Preusse et al. (2014), and that was already previously applied to high-resolution model data (Preusse et al., 2014; Stephan et al., 2019a, 2019b; Strube et al., 2021), as well as observations of GWs by aircraft (e.g., Krisch et al., 2017; Krisch et al., 2020) and by the AIRS satellite instrument (Ern et al., 2017). For the S3D method, a larger 3D data set is subdivided into smaller subvolumes. In these subvolumes, 3D sinusoidal fits are performed that provide amplitude and 3D wave vector of the fitted waves. Like in Ern et al. (2017), we use subvolumes of $17 \times 17 \times 7$ AIRS data points along-track × across-track × vertical, corresponding to an approximate size of about $300 \times 200 \times 18$ km^3 at nadir. We consider the strongest two wave components in each fit volume. In order to focus on the fits that can reliably be performed with the chosen sub-volume size, we discard all fits resulting in horizontal wavelengths >700 km and vertical wavelengths >50 km, that is, all fits resulting in wavelengths exceeding the fit volume size by more than a factor of about 2–3. Otherwise, fits could lead to runaway amplitudes. In addition, all GW amplitudes <0.4 K are set to zero to avoid contamination of the results by noise.

In a first step, for the consecutive days 13–16 January 2022 we compare GW amplitudes of the two S3D fit components combined. Results are shown in Figures 1d–1g for the Southern Hemisphere at an altitude of 36 km.

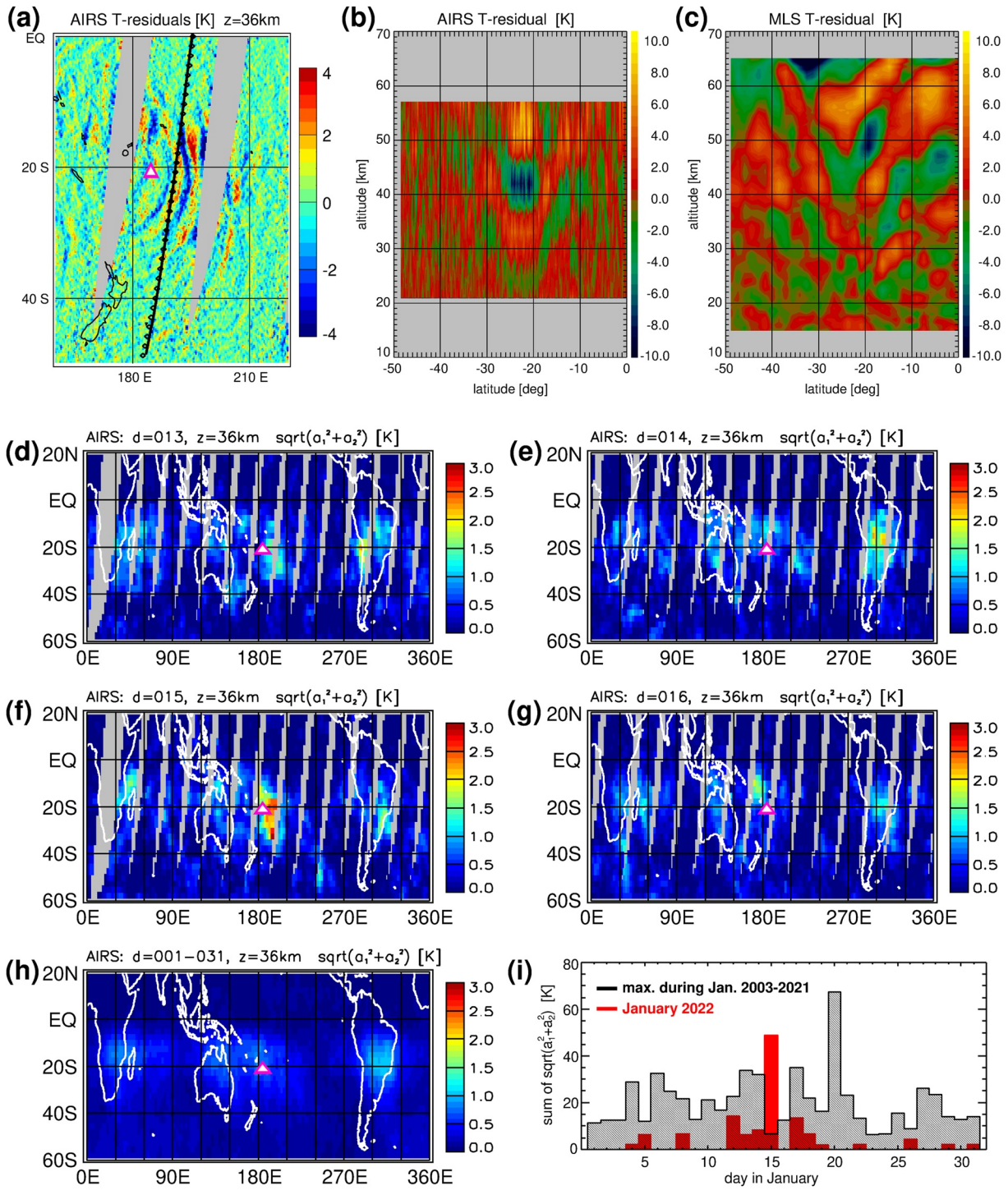

Figure 1. (a) Horizontal distribution of AIRS residual temperatures in the Tonga area on 15 January 2022. Values are on a 0.25° × 0.25° longitude-latitude grid and obtained by averaging in overlapping 0.5° × 0.5° intervals. The positions of individual MLS soundings are marked with black diamonds, and the black line indicates the position of the AIRS footprint track that best coincides with MLS. Panel (b) shows the latitude-altitude section of residual temperatures observed by AIRS along the black line marked in (a), while (c) shows the same as (b), but for MLS observations at the positions of the black diamonds in (a). Panels (d)–(g) show southern hemisphere AIRS GW amplitudes of the two S3D fit components combined for the consecutive days 13–16 January 2022, and (h) averaged over January 2022. Values are on a 2.5° × 2.5° longitude-latitude grid and obtained by averaging in overlapping 5° × 5° intervals. In the maps the position of the volcano is marked with a magenta triangle. Panel (i) shows the cumulative sum of AIRS GW amplitudes exceeding a threshold of 2.0 K for each day in January 2022 (red histogram), and the maximum cumulative sum on the respective day in January determined from the single years of the period 2003–2021 (black histogram). The respective sums were taken over all grid points at 36 km in the whole area shown in (d)–(h).

Obviously, the GW event on 15 January in the Tonga area is the strongest event seen by AIRS in the time period considered, and it is also much stronger than the average amplitudes in January 2022 in the Southern Hemisphere (Figure 1h).

To further confirm that the event on 15 January 2022 was exceptional for AIRS, Figure 1i shows the cumulative sum of AIRS GW amplitudes exceeding a threshold of 2.0 K for each day in January 2022 (red histogram), and the maximum cumulative sum on the respective day in January determined from the single years of the period 2003–2021 (black histogram). The respective sums were taken over all grid points at 36 km in the whole area shown in Figures 1d–1h. As can be seen from Figure 1i, the event on 15 January 2022 was stronger than the strongest events on any day in January in any year of the period 2003–2022, except for 20 January 2013 when the combination of two strong convective GW events at the coasts of South America and Africa led to somewhat higher cumulative values than the single event on 15 January 2022 caused by the Tonga volcano.

In a second step, we investigate the wave parameters of the strongest S3D fit component in each S3D fit subvolume. The results are shown in Figures 2a–2c for an altitude of 36 km for GW amplitudes (Figure 2a), horizontal wavelengths (Figure 2b), and vertical wavelengths (Figure 2c). As can be seen from Figures 2a–2c, the amplitude of the Tonga wave event is about 2–3 K, the horizontal wavelength approximately 500 km, and the vertical wavelength somewhat above 20 km.

Around (35°S, 205°E) there is a region of exceptionally long vertical wavelengths (λ_z of approximately 40 km). This event is observed in the orbit preceding the main event (i.e., approximately 100 min earlier). This event may also be related to the volcanic eruption. The different wave characteristics suggest that this is a different wave, and not the same wave seen in an earlier orbit. This would confirm that GWs of different wave characteristics were excited by the eruption.

Next, we calculate GWMF to investigate whether the wave event could have stronger effect on the global-scale background winds. GWMF is an important parameter because its vertical gradients is proportional to the forcing (acceleration, or deceleration) of the background winds (e.g., Fritts & Alexander, 2003). GWMF can be calculated from observed GW temperature amplitudes (e.g., Ern et al., 2004; Ern et al., 2017):

$$(F_{px}, F_{py}) = \frac{1}{2}\,\varrho\,\frac{(k,l)}{m}\left(\frac{g}{N}\right)^2\left(\frac{\hat{T}}{T}\right)^2 \tag{1}$$

Here, F_{px} and F_{py} are the zonal and meridional GWMF, respectively, (k, l, m) is the vector of zonal, meridional and vertical GW wave numbers, $\hat{T}$ the GW temperature amplitude, g Earth's gravity acceleration, N the buoyancy frequency, ϱ the atmospheric background density, and T the atmospheric background temperature. In addition, absolute values (F_{ph}) of GWMF can be calculated using the horizontal and vertical wavelength of a GW:

$$F_{ph} = \frac{1}{2}\,\varrho\,\frac{\lambda_z}{\lambda_h}\left(\frac{g}{N}\right)^2\left(\frac{\hat{T}}{T}\right)^2 \tag{2}$$

For both S3D fit components combined, Figure 2 shows in the vicinity of the GW event also GW squared amplitudes (Figure 2d), zonal GWMF (Figure 2e), meridional GWMF (Figure 2f), and absolute GWMF (Figure 2g). The main event has peak absolute GWMF of approximately 3 mPa. Zonal GWMF is directed eastward, that is, opposite to the stratospheric background winds. Remarkably, meridional GWMF east of the volcano is directed northward north of the volcano, and southward south of it, further confirming the volcanic eruption as the source of the GW event. As mentioned before, during the period considered, this event is the strongest seen by AIRS in the Southern Hemisphere, and of comparable strength to the GWMF seen by AIRS in the northern hemisphere polar night jet (e.g., Ern et al., 2017; Hindley et al., 2020), but much weaker than the Southern Andes hotspot of GWs during austral winter (e.g., Ern et al., 2018; Hindley et al., 2020). It should be noted, however, that the combination of the AIRS visibility filter and the chosen S3D analysis volume size leads to sensitivity for waves of 100–700 km horizontal wavelengths and 15–50 km vertical wavelengths only.

3.2.2. MLS Observations

MLS GW amplitudes are determined similar as described in Ern et al. (2004) and Ern et al. (2011, 2018). Sinusoidal fits are performed for each temperature altitude profile in sliding vertical windows of 12 km vertical extent (Preusse et al., 2002). Global distributions of MLS GW squared amplitudes in the Southern Hemisphere are

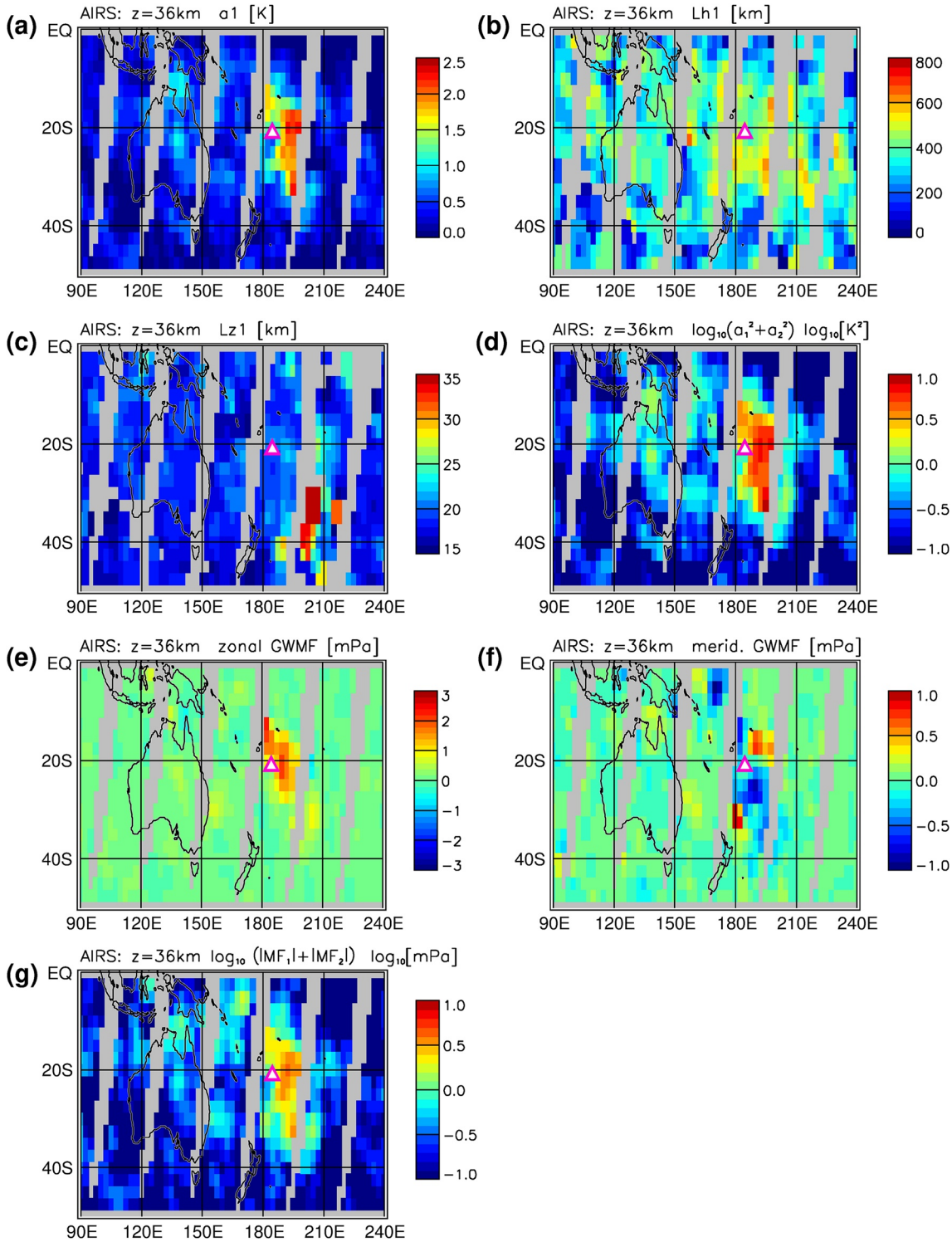

Figure 2. Horizontal distributions on 15 January 2022 at 36 km altitude in the Tonga area for the strongest S3D fit component in each fitting volume: (a) AIRS GW amplitudes, (b) GW horizontal wavelengths, and (c) vertical wavelengths, and for both S3D fit components in each fitting volume combined: (d) GW squared amplitudes, (e) zonal GWMF, (f) meridional GWMF, and (g) absolute GWMF. Values are on a 2.5° × 2.5° longitude-latitude grid and obtained by averaging in overlapping 5° × 5° intervals. The position of the volcano is marked with a magenta triangle.

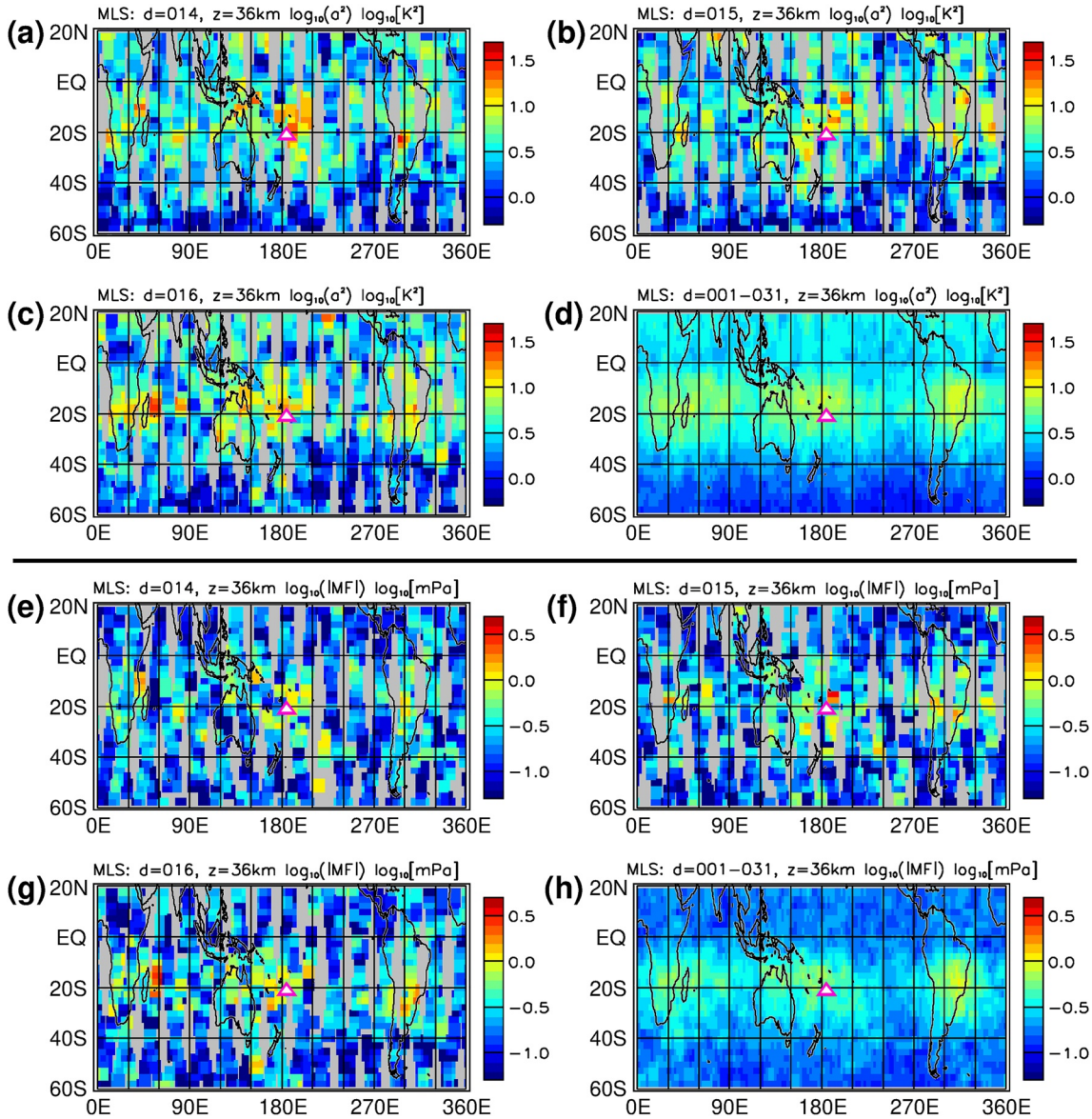

Figure 3. Horizontal distributions at 36 km altitude of MLS GW squared amplitudes for (a)–(c) 14–16 January 2022 and (d) averaged over January 2022. Panels (e)–(h) show the same as (a)–(d), but for MLS absolute GWMF. Values are on a 2.5° × 2.5° longitude-latitude grid and obtained by averaging in overlapping 10° × 5° intervals. The position of the volcano is marked with a magenta triangle.

shown in Figures 3a–3c at 36 km altitude for the consecutive days 14–16 January 2022, and averaged over January 2022 (Figure 3d). As can be seen, several values of large GW squared amplitudes (up to approximately 20 K^2) are found in the vicinity of Tonga on 15 January. However, compared to other regions and other days in the Southern Hemisphere, these are not exceptionally strong, but stronger than the January 2022 average. Please note that due to the different observational filters, MLS squared amplitudes are usually larger than for AIRS. Please also note that the global GW distribution is very intermittent (e.g., Hertzog et al., 2012). This means that single events can exceed average distributions by far, and this is why a comparison of the distribution for 15 January 2022 with other single-day GW distributions is more meaningful than the comparison with the January average distribution.

From the 2D information provided by the single MLS measurement track, it is not possible to calculate directional GWMF. Still, we can calculate absolute GWMF from MLS observations by estimating the along-track horizontal wavelength from phase differences between consecutive altitude profiles. This along-track wavelength is taken as a proxy for the true GW horizontal wavelength (λ_h). Of course, this will introduce large uncertainties

and absolute GWMF is likely underestimated (e.g., Ern et al., 2004; Ern et al., 2018; Preusse et al., 2009). The MLS absolute GWMF shown in Figures 3e–3h basically confirms the findings from MLS squared amplitudes. Still, there are enhanced values of approximately 4 mPa on 15 January northeast of the volcano in the MLS orbit crossing the GW event.

4. Ray Tracing of Gravity Waves

To further investigate the origin of the wave event observed on 15 January, we initialize the Gravity wave Regional Or Global Ray Tracer (GROGRAT; Eckermann & Marks, 1997; Marks & Eckermann, 1995) on 15 January at an altitude of 36 km with GW amplitudes and directions using the gridded AIRS S3D results shown in Figure 2 for the strongest S3D fit component. In addition, we here use also the second fit component. These GW fit results are traced backward and forward in time. For this, we use 3-hourly data of NASA's Modern-Era Retrospective analysis for Research and Applications, version 2 (MERRA-2) reanalysis (Gelaro et al., 2017) as background atmosphere.

The results are shown in Figure 4. Figure 4a shows the starting points of the ray traces at an altitude of 36 km, color-coded with their start amplitude (only strongest S3D fit component shown). Figure 4b shows the end points of all backward ray traces (including second fit component), also color-coded by their starting amplitude at 36 km. The rays are traced backward in time as far as possible, that is, until reaching Earth's surface, or reaching critical levels (resulting in $m \rightarrow 0$, and vertical group velocity approaching zero). Obviously, the back-tracing end points of the largest-amplitude starting points group in close vicinity to the location of the volcano (magenta triangle). The average wave propagation time of these backward rays is between 3 and 12 hr, that is, they bracket the onset time of the volcanic eruption with an average of approximately 2 hr after the eruption. This is clear evidence of the eruption being the source of the GW event.

Figure 4c shows the ray-paths of all rays that pass the location of the volcano closer than a radius of 200 km during backtracing. The ray-paths are color-coded by their altitude during wave propagation. Remarkably, many rays pass the location of the volcano at altitudes of 10 km and below, but some rays pass this location at higher altitudes (up to approximately 25 km), indicating that the source of the GW is not only near the surface, but the wave is excited over a larger range of altitudes. This could also be expected because the volcanic plume extended well into the stratosphere. The results of forward ray tracing in Figure 4c indicate that, starting from 36 km, the wave did not travel larger distances while propagating upward, and it reached an altitude of approximately 70 km already approximately 2 hr after the observation at 36 km altitude. The ray tracing was limited to altitudes below 70 km because the MERRA-2 model top is only somewhat above 70 km.

Also shown in Figures 4d–4f is the variation of GW horizontal wavelengths, amplitudes, and vertical wavelengths with altitude for GW ray traces that have launch amplitudes >1 K (corresponding to approximately ∼2 m/s) at 36 km (see Figure 4a). Figures 4g–4i show the same wave parameters taken from the S3D fits at the longitude and latitude where the respective ray intersects the AIRS swath at a given altitude. Comparison of the ray traces with the AIRS S3D results shows good qualitative agreement. Minor deviations can be attributed to the fact that S3D results represent an average over 18 km. Further, values at the highest and lowest altitudes may partly be noise-affected.

5. Conclusions

On 15 January 2022, a major eruption of the Hunga Tonga–Hunga Ha'apai volcano happened. This eruption was likely the strongest worldwide for decades, and it triggered a broad spectrum of atmospheric waves (e.g., Lamb waves and gravity waves [GWs]). In our study we focus on the mesoscale response. About 8.5 hr after the event a strong GW was observed in AIRS and MLS satellite data. Using AIRS data as input, we traced the GW backward in time with the GROGRAT GW ray tracer, and we confirmed the volcanic eruption as the wave source. It is indicated that the wave source extended from near-ground into the lower stratosphere. Horizontal and vertical wavelengths of the GW are approximately 500 and 20 km, respectively. Squared GW amplitudes are approximately 5 K^2 for AIRS and up to 15 K^2 for MLS. Absolute GWMF is approximately 3 mPa for AIRS and up to 4 mPa for MLS. In AIRS observations this GW was one of the strongest seen in the Southern Hemisphere in January 2022. In MLS, which has a somewhat wider observational filter than AIRS, the event was also strong,

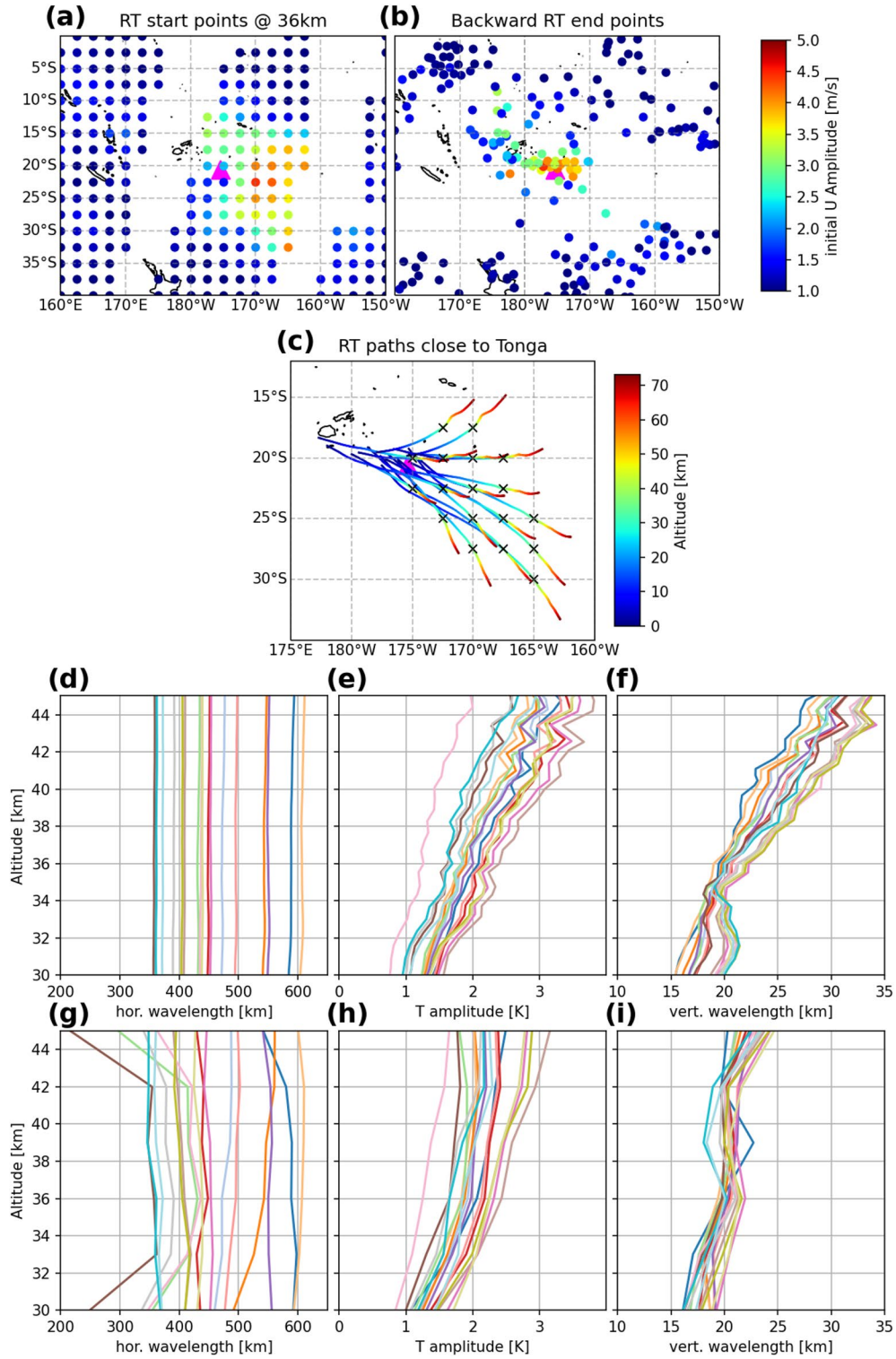

Figure 4. Shown are (a) the starting points of ray-traces using S3D fit results of AIRS data on 15 January 2022, (b) end points of the backward ray traces, and (c) the ray-paths of those rays that pass the volcano (magenta triangle) at a distance closer than 200 km. Points in (a) and (b) are color-coded by their launch amplitude at 36 km (in (a) only the strongest S3D fit component, in (b) both components). Ray-paths in (c) are color-coded by their altitude during GW propagation, and the ray starting points at 36 km altitude are marked with black crosses. Panels (d)–(f) show GW horizontal wavelengths, amplitudes, and vertical wavelengths versus altitude of ray traces for rays with launch amplitude >1 K at 36 km. Panels (g)–(i) shows the same as (d)–(f), but for the AIRS S3D results at the position of the respective ray. In panels (d)–(i) the same color refers to the same ray.

but not as exceptional as in AIRS data. Our amplitude and GWMF estimates should be low-biased due to the observational filters of the instruments and due to the limitations of our analysis methods. Therefore, it is also likely that considerable GWMF may be found at GW horizontal wavelengths <100 km. Still, it is not expected that this single short-lived event will have stronger effect on the large-scale atmospheric circulation. Nevertheless, we consider the event highly interesting for future studies of high-resolution upper atmosphere modeling, and for more in-depth observational studies.

Appendix A: Determination of Temperature Fluctuations Due To GWs

To obtain temperature fluctuations that can be attributed to small-scale GWs, the large-scale background is removed from the AIRS temperatures by subtracting a fourth-order polynomial fit in across-track direction. This method has already been used in several AIRS studies (e.g., Alexander & Teitelbaum, 2007; Ern et al., 2017; Hoffmann et al., 2014; Wright et al., 2017).

For MLS, temperature fluctuations due to small-scale GWs are obtained as described in Ern et al. (2011) and Ern et al. (2013, 2018). In a first step, for a set of fixed latitudes (every full degree) and altitudes (every full kilometer), 2D spectra in longitude and time are calculated for a set of overlapping time-windows of 31 days length. These spectra are back-transformed into physical space for the largest spectral components (that can be attributed to global-scale waves) at the exact longitude and time of each MLS observation. Then, this estimate of the large-scale background temperature is subtracted from each MLS observation. In this procedure, global-scale waves with periods >1.3 days are considered. In a second step, global-scale tidal modes are removed. MLS observations are at two fixed LSTs: one LST corresponding to ascending, the other LST to descending orbit parts. Therefore, tides appear as stationary wave patterns if ascending and descending orbit parts are considered separately. The major tidal modes are removed by determining these stationary waves up to zonal wave number 4 and subtracting them from the temperature residuals obtained after the first step. The remaining temperature fluctuations are then attributed to small-scale GWs.

Different from the procedure described in Ern et al. (2011) and Ern et al. (2013, 2018), we do not apply additional high-pass filtering of temperature altitude profiles, such that the full range of GW vertical wavelengths contained in MLS data is kept. This high-pass filtering step is not necessary here because for determining GW amplitudes from MLS observations we use larger sliding vertical windows of 12 km vertical extent that allow to characterize also GWs of λ_z up to 30 km. Further, in the summer hemisphere stratosphere the activity of planetary waves is very weak, and the cleanup-effect of this filter is not needed to remove remnants of global-scale waves remaining after the first step.

Data Availability Statement

Aura-MLS version 5.01 geopotential height data (M. J. Schwartz, 2008; Livesey et al., 2022) are provided by M. Schwartz et al. (2020a) and are available at https://acdisc.gesdisc.eosdis.nasa.gov/data/Aura_MLS_Level2/ML2GPH.005. Aura-MLS version 5.01 temperature data (M. J. Schwartz, 2008; Livesey et al., 2022) are provided by M. Schwartz et al. (2020b) and are available at https://acdisc.gesdisc.eosdis.nasa.gov/data/Aura_MLS_Level2/ML2T.005. MERRA-2 reanalysis data (Gelaro et al., 2017) are provided by Global Modeling and Assimilation Office (GMAO, 2015) and are available at: https://doi.org/10.5067/WWQSXQ8IVFW8. AIRS temperature retrieval data (L. Hoffmann & Alexander, 2009) are provided by Hoffmann (2022) and are available at: https://datapub.fz-juelich.de/slcs/airs/gravity_waves/data/projects/tonga.

Acknowledgments
ME was supported by the German Federal Ministry of Education and Research (BMBF) grant 01LG1905C (QUBICC, ROMIC). Open access funding enabled and organized by Projekt DEAL.

References

Adam, D. (2022). Tonga volcano eruption created puzzling ripples in Earth's atmosphere. *Nature*, *601*, 497. https://doi.org/10.1038/d41586-022-00127-1

Alexander, M. J., & Dunkerton, T. J. (1999). A spectral parameterization of mean-flow forcing due to breaking gravity waves. *Journal of the Atmospheric Sciences*, *56*, 4167–4182. https://doi.org/10.1175/1520-0469(1999)056<4167:aspomf>2.0.co;2

Alexander, M. J., Geller, M., McLandress, C., Polavarapu, S., Preusse, P., Sassi, F., et al. (2010). Recent developments in gravity-wave effects in climate models and the global distribution of gravity-wave momentum flux from observations and models. *Quarterly Journal of the Royal Meteorological Society*, *136*, 1103–1124. https://doi.org/10.1002/qj.637

Alexander, M. J., Holton, J. R., & Durran, D. R. (1995). The gravity wave response above deep convection in a squall line simulation. *Journal of the Atmospheric Sciences*, *52*, 2212–2226. https://doi.org/10.1175/1520-0469(1995)052<2212:tgwrad>2.0.co;2

Alexander, M. J., & Teitelbaum, H. (2007). Observation and analysis of a large amplitude mountain wave event over the Antarctic Peninsula. *Journal of Geophysical Research*, *112*. https://doi.org/10.1029/2006JD008368

Aumann, H. H., Chahine, M. T., Gautier, C., Goldberg, M. D., Kalnay, E., McMillin, L. M., et al. (2003). AIRS/AMSU/HSB on the Aqua mission: Design, science objective, data products, and processing systems. *IEEE Transactions on Geoscience and Remote Sensing*, *41*, 253–264. https://doi.org/10.1109/TGRS.2002.808356

Baldwin, M. P., Gray, L. J., Dunkerton, T. J., Hamilton, K., Haynes, P. H., Randel, W. J., et al. (2001). The quasi-biennial oscillation. *Reviews of Geophysics*, *39*, 179–229. https://doi.org/10.1029/1999RG000073

Beres, J. H., Garcia, R. R., Boville, B. A., & Sassi, F. (2005). Implementation of a gravity wave source spectrum parameterization dependent on the properties of convection in the Whole Atmosphere Community Climate Model (WACCM). *Journal of Geophysical Research*, *110*, D10108. https://doi.org/10.1029/2004JD005504

Chahine, M. T., Pagano, T. S., Aumann, H. H., Atlas, R., Barnet, C., Blaisdell, J., et al. (2006). AIRS: Improving weather forecasting and providing new data on greenhouse gases. *Bulletin of the American Meteorological Society*, *87*(7), 911–926. https://doi.org/10.1175/BAMS-87-7-911

Cho, C., & Staelin, D. H. (2006). Cloud clearing of Atmospheric Infrared Sounder hyperspectral infrared radiances using stochastic methods. *Journal of Geophysical Research*, *111*, D09518. https://doi.org/10.1029/2005JD006013

Chun, H.-Y., & Baik, J.-J. (1998). Momentum flux by thermally induced internal gravity waves and its approximation for large-scale models. *Journal of the Atmospheric Sciences*, *55*, 3299–3310. https://doi.org/10.1175/1520-0469(1998)055<3299:mfbtii>2.0.co;2

Eckermann, S. D., & Marks, C. J. (1997). GROGRAT: A new model of the global propagation and dissipation of atmospheric gravity waves. *Advances in Space Research*, *20*, 1253–1256. https://doi.org/10.1016/s0273-1177(97)00780-1

Eckermann, S. D., & Preusse, P. (1999). Global measurements of stratospheric mountain waves from space. *Science*, *286*(5444), 1534–1537. https://doi.org/10.1126/science.286.5444.1534

Ern, M., Diallo, M., Preusse, P., Mlynczak, M. G., Schwartz, M. J., Wu, Q., & Riese, M. (2021). The semiannual oscillation (SAO) in the tropical middle atmosphere and its gravity wave driving in reanalyses and satellite observations. *Atmospheric Chemistry and Physics*, *21*, 13763–13795. https://doi.org/10.5194/acp-21-13763-2021

Ern, M., Hoffmann, L., & Preusse, P. (2017). Directional gravity wave momentum fluxes in the stratosphere derived from high-resolution AIRS temperature data. *Geophysical Research Letters*, *44*(1), 475–485. https://doi.org/10.1002/2016GL072007

Ern, M., Ploeger, F., Preusse, P., Gille, J. C., Gray, L. J., Kalisch, S., et al. (2014). Interaction of gravity waves with the QBO: A satellite perspective. *Journal of Geophysical Research: Atmospheres*, *119*, 2329–2355. https://doi.org/10.1002/2013JD020731

Ern, M., Preusse, P., Alexander, M. J., & Warner, C. D. (2004). Absolute values of gravity wave momentum flux derived from satellite data. *Journal of Geophysical Research*, *109*(D20), D20103. https://doi.org/10.1029/2004JD004752

Ern, M., Preusse, P., Gille, J. C., Hepplewhite, C. L., Mlynczak, M. G., Russell, J. M., III, & Riese, M. (2011). Implications for atmospheric dynamics derived from global observations of gravity wave momentum flux in stratosphere and mesosphere. *Journal of Geophysical Research*, *116*, D19107. https://doi.org/10.1029/2011JD015821

Ern, M., Preusse, P., Kalisch, S., Kaufmann, M., & Riese, M. (2013). Role of gravity waves in the forcing of quasi two-day waves in the mesosphere: An observational study. *Journal of Geophysical Research: Atmospheres*, *118*(9), 3467–3485. https://doi.org/10.1029/2012JD018208

Ern, M., Preusse, P., & Riese, M. (2015). Driving of the SAO by gravity waves as observed from satellite. *Annales Geophysicae*, *33*(4), 483–504. https://doi.org/10.5194/angeo-33-483-2015

Ern, M., Trinh, Q. T., Preusse, P., Gille, J. C., Mlynczak, M. G., Russell, J. M., III, & Riese, M. (2018). GRACILE: A comprehensive climatology of atmospheric gravity wave parameters based on satellite limb soundings. *Earth System Science Data*, *10*, 857–892. https://doi.org/10.5194/essd-10-857-2018

Fritts, D., & Alexander, M. (2003). Gravity wave dynamics and effects in the middle atmosphere. *Reviews of Geophysics*, *41*(1). https://doi.org/10.1029/2001RG000106

Gelaro, R., McCarty, W., Suárez, M. J., Todling, R., Molod, A., Takacs, L., et al. (2017). The Modern-Era Retrospective Analysis for Research and Applications, Version 2 (MERRA-2). *Journal of Climate*, *30*(14), 5419–5454. https://doi.org/10.1175/jcli-d-16-0758.1

Global Modeling and Assimilation Office (GMAO). (2015). MERRA-2 inst3_3d_asm_Nv: 3D, 3-hourly, instantaneous, model-level, assimilation. Assimilated Meteorological Fields V5.12.4 [Dataset]. Goddard Earth Sciences Data and Information Services Center (GES DISC). https://doi.org/10.5067/WWQSXQ8IVFW8

Global Volcanism Program. (2022). Report on Hunga Tonga-Hunga Ha'apai (Tonga). In S. K. Sennert (Ed.), *Weekly volcanic activity report, 12 January-18 January 2022*. Smithsonian Institution and US Geological Survey. Retrieved from https://volcano.si.edu/showreport.cfm?doi=GVP.WVAR20220112-243040

Gong, J., Wu, D. L., & Eckermann, S. D. (2012). Gravity wave variances and propagation derived from AIRS radiances. *Atmospheric Chemistry and Physics*, *12*(4), 1701–1720. https://doi.org/10.5194/acp-12-1701-2012

Gong, J., Yue, J., & Wu, D. L. (2015). Global survey of concentric gravity waves in AIRS images and ECMWF analysis. *Journal of Geophysical Research: Atmospheres*, *120*(6), 2210–2228. https://doi.org/10.1002/2014JD022527

Gossard, E. E., & Hooke, W. H. (1975). *Waves in the atmosphere, atmospheric infrasound and gravity waves - their generation and propagation*. Elsevier Scientific Publishing Company.

Hamilton, K., & Mahlman, J. (1988). General-circulation model simulation of the semiannual oscillation of the tropical middle atmosphere. *Journal of the Atmospheric Sciences*, *45*, 3212–3235. https://doi.org/10.1175/1520-0469(1988)045<3212:gcmsot>2.0.co;2

Hertzog, A., Alexander, M. J., & Plougonven, R. (2012). On the intermittency of gravity wave momentum flux in the stratosphere. *Journal of the Atmospheric Sciences*, *69*(11), 3433–3448. https://doi.org/10.1175/JAS-D-12-09.1

Hindley, N. P., Wright, C. J., Hoffmann, L., Moffat-Griffin, T., & Mitchell, N. J. (2020). An 18-year climatology of directional stratospheric gravity wave momentum flux from 3-D satellite observations. *Geophysical Research Letters*, *47*(22), e2020GL089557. https://doi.org/10.1029/2020GL089557

Hoffmann, L. (2022). AIRS/Aqua observations of stratospheric gravity waves of the January 2022 Hunga Tonga-Hunga Ha'apai volcano eruption [Dataset]. Jülich DATA, V1. https://doi.org/10.26165/JUELICH-DATA/DWABVZ

Hoffmann, L., & Alexander, M. J. (2009). Retrieval of stratospheric temperatures from Atmospheric Infrared Sounder radiance measurements for gravity wave studies. *Journal of Geophysical Research*, *114*, D07105. https://doi.org/10.1029/2008JD011241

Hoffmann, L., Alexander, M. J., Clerbaux, C., Grimsdell, A. W., Meyer, C. I., Rößler, T., & Tournier, B. (2014). Intercomparison of stratospheric gravity wave observations with AIRS and IASI. *Atmospheric Measurement Techniques*, *7*(12), 4517–4537. https://doi.org/10.5194/amt-7-4517-2014

Hoffmann, L., Xue, X., & Alexander, M. J. (2013). A global view of stratospheric gravity wave hotspots located with Atmospheric Infrared Sounder observations. *Journal of Geophysical Research: Atmospheres*, *118*(2), 416–434. https://doi.org/10.1029/2012JD018658

Holton, J. R. (1983). The influence of gravity wave breaking on the general circulation of the middle atmosphere. *Journal of the Atmospheric Sciences*, *40*, 2497–2507. https://doi.org/10.1175/1520-0469(1983)040<2497:tiogwb>2.0.co;2

Jiang, J., Eckermann, S., Wu, D., & Ma, J. (2004). A search for mountain waves in MLS stratospheric limb radiances from the winter Northern Hemisphere: Data analysis and global mountain wave modeling. *Journal of Geophysical Research*, *109*(D3), D03107. https://doi.org/10.1029/2003JD003974

Krisch, I., Ern, M., Hoffmann, L., Preusse, P., Strube, C., Ungermann, J., et al. (2020). Superposition of gravity waves with different propagation characteristics observed by airborne and space-borne infrared sounders. *Atmospheric Chemistry and Physics*, *20*(19), 11469–11490. https://doi.org/10.5194/acp-20-11469-2020

Krisch, I., Preusse, P., Ungermann, J., Dörnbrack, A., Eckermann, S. D., Ern, M., et al. (2017). First tomographic observations of gravity waves by the infrared limb imager GLORIA. *Atmospheric Chemistry and Physics*, *17*(24), 14937–14953. https://doi.org/10.5194/acp-17-14937-2017

Kruse, C. G., Alexander, M. J., Hoffmann, L., van Niekerk, A., Polichtchouk, I., Bacmeister, J., et al. (2022). Observed and modeled mountain waves from the surface to the mesosphere near the Drake Passage. *Journal of the Atmospheric Sciences*, *79*, 909–932. https://doi.org/10.1175/JAS-D-21-0252.1

Lane, T. P., Reeder, M. J., & Clark, T. L. (2001). Numerical modeling of gravity wave generation by deep tropical convection. *Journal of the Atmospheric Sciences*, *58*, 1249–1274. https://doi.org/10.1175/1520-0469(2001)058<1249:nmogwg>2.0.co;2

Lehmann, C. I., Kim, Y.-H., Preusse, P., Chun, H.-Y., Ern, M., & Kim, S.-Y. (2012). Consistency between Fourier transform and small-volume few-wave decomposition for spectral and spatial variability of gravity waves above a typhoon. *Atmospheric Measurement Techniques*, *5*(7), 1637–1651. https://doi.org/10.5194/amt-5-1637-2012

Lindzen, R. S., & Holton, J. R. (1968). A theory of the quasi-biennial oscillation. *Journal of the Atmospheric Sciences*, *25*(6), 1095–1107. https://doi.org/10.1175/1520-0469(1968)025<1095:atotqb>2.0.co;2

Livesey, N. J., Read, W. G., Wagner, P. A., Froidevaux, L., Santee, M. L., Schwartz, M. J., & Lay, R. R. (2022). *Earth Observing System (EOS) Aura Microwave Limb Sounder (MLS) version 5.0x level 2 and 3 data quality and description document Version 5.0–1.1a (Tech. Rep.)*. Jet Propulsion Laboratory, California Institute of Technology. Retrieved from https://mls.jpl.nasa.gov/data/v5-0_data_quality_document.pdf

Marks, C. J., & Eckermann, S. D. (1995). A three-dimensional nonhydrostatic ray-tracing model for gravity waves: Formulation and preliminary results for the middle atmosphere. *Journal of the Atmospheric Sciences*, *52*, 1959–1984. https://doi.org/10.1175/1520-0469(1995)052<1959:atdnrt>2.0.co;2

Meyer, C. I., Ern, M., Hoffmann, L., Trinh, Q. T., & Alexander, M. J. (2018). Intercomparison of AIRS and HIRDLS stratospheric gravity wave observations. *Atmospheric Measurement Techniques*, *11*(1), 215–232. https://doi.org/10.5194/amt-11-215-2018

Piani, C., Durran, D., Alexander, M. J., & Holton, J. R. (2000). A numerical study of three-dimensional gravity waves triggered by deep tropical convection and their role in the dynamics of the QBO. *Journal of the Atmospheric Sciences*, *57*, 3689–3702. https://doi.org/10.1175/1520-0469(2000)057<3689:ansotd>2.0.co;2

Plougonven, R., & Zhang, F. (2014). Internal gravity waves from atmospheric jets and fronts. *Reviews of Geophysics*, *52*(1), 33–76. https://doi.org/10.1002/2012RG000419

Poli, P., & Shapiro, N. M. (2022). Rapid characterization of large volcanic eruptions: Measuring the impulse of the Hunga Tonga Ha'apai explosion from teleseismic waves. *Geophysical Research Letters*, *49*(8), e2022GL098123. https://doi.org/10.1029/2022GL098123

Preusse, P., Dörnbrack, A., Eckermann, S. D., Riese, M., Schaeler, B., Bacmeister, J. T., et al. (2002). Space-based measurements of stratospheric mountain waves by CRISTA, 1. Sensitivity, analysis method, and a case study. *Journal of Geophysical Research*, *107*(D23), 8178–8181. https://doi.org/10.1029/2001JD000699

Preusse, P., Eckermann, S. D., & Ern, M. (2008). Transparency of the atmosphere to short horizontal wavelength gravity waves. *Journal of Geophysical Research*, *113*, D24104. https://doi.org/10.1029/2007JD009682

Preusse, P., Ern, M., Bechtold, P., Eckermann, S. D., Kalisch, S., Trinh, Q. T., & Riese, M. (2014). Characteristics of gravity waves resolved by ECMWF. *Atmospheric Chemistry and Physics*, *14*(19), 10483–10508. https://doi.org/10.5194/acp-14-10483-2014

Preusse, P., Schroeder, S., Hoffmann, L., Ern, M., Friedl-Vallon, F., Ungermann, J., et al. (2009). New perspectives on gravity wave remote sensing by spaceborne infrared limb imaging. *Atmospheric Measurement Techniques*, *2*(1), 299–311. https://doi.org/10.5194/amt-2-299-2009

Radio New Zealand. (2022). *Tonga eruption likely the world's largest in 30 years - scientist*. Retrieved from https://www.rnz.co.nz/news/world/459657/tonga-eruption-likely-the-world-s-largest-in-30-years-scientist (interview with Volcanologist Professor Shane Cronin of the University of Auckland and NIWA tsunami expert Dr. Emily Lane; last access: 23 February 2022)

Schwartz, M., Livesey, N., & Read, W. (2020a). MLS/Aura level 2 geopotential height V005 [Dataset]. Goddard Earth Sciences Data and Information Services Center (GES DISC). https://doi.org/10.5067/Aura/MLS/DATA2507

Schwartz, M., Livesey, N., & Read, W. (2020b). MLS/Aura level 2 temperature V005[Dataset]. Goddard Earth Sciences Data and Information Services Center (GES DISC). https://doi.org/10.5067/Aura/MLS/DATA2520

Schwartz, M. J., Lambert, A., Manney, G. L., Read, W. G., Livesey, N. J., Froidevaux, L., et al. (2008). Validation of the Aura Microwave Limb Sounder temperature and geopotential height measurements. *Journal of Geophysical Research*, *113*, D15S11. https://doi.org/10.1029/2007JD008783

Stephan, C. C., Strube, C., Klocke, D., Ern, M., Hoffmann, L., Preusse, P., & Schmidt, H. (2019a). Gravity waves in global high-resolution simulations with explicit and parameterized convection. *Journal of Geophysical Research: Atmospheres*, *124*(8), 4446–4459. https://doi.org/10.1029/2018JD030073

Stephan, C. C., Strube, C., Klocke, D., Ern, M., Hoffmann, L., Preusse, P., & Schmidt, H. (2019b). Intercomparison of gravity waves in global convection-permitting models. *Journal of the Atmospheric Sciences*, *76*(9), 2739–2759. https://doi.org/10.1175/JAS-D-19-0040.1

Strube, C., Preusse, P., Ern, M., & Riese, M. (2021). Propagation paths and source distributions of resolved gravity waves in ECMWF-IFS analysis fields around the southern polar night jet. *Atmospheric Chemistry and Physics*, *21*(24), 18641–18668. https://doi.org/10.5194/acp-21-18641-2021

Susskind, J., Barnett, C. D., & Blaisdell, J. M. (2003). Retrieval of atmospheric and surface parameters from AIRS/AMSU/HSB data in the presence of clouds. *IEEE Transactions on Geoscience and Remote Sensing*, *41*, 390–409. https://doi.org/10.1109/tgrs.2002.808236

Trinh, Q. T., Kalisch, S., Preusse, P., Ern, M., Chun, H.-Y., Eckermann, S. D., et al. (2016). Tuning of a convective gravity wave source scheme based on HIRDLS observations. *Atmospheric Chemistry and Physics*, *16*, 7335–7356. https://doi.org/10.5194/acp-16-7335-2016

USGS Earthquakes Hazards Program. (2022). *M 5.8 volcanic eruption - 68 km NNW of Nuku'alofa, Tonga*. Retrieved from https://earthquake.usgs.gov/earthquakes/eventpage/us7000gc8r/executive

Waters, J., Froidevaux, L., Harwood, R., Jarnot, R., Pickett, H., Read, W., et al. (2006). The Earth Observing System Microwave Limb Sounder (EOS MLS) on the Aura satellite. *IEEE Transactions on Geoscience and Remote Sensing*, *44*(5), 1075–1092. https://doi.org/10.1109/TGRS.2006.873771

Wright, C. J., Hindley, N. P., Alexander, M. J., Barlow, M., Hoffmann, L., Mitchell, C. N., et al. (2022). Tonga eruption triggered waves propagating globally from surface to edge of space. *Earth and Space Science Open Archive (ESSOAr) - Preprint server*. https://doi.org/10.1002/essoar.10510674.1

Wright, C. J., Hindley, N. P., Hoffmann, L., Alexander, M. J., & Mitchell, N. J. (2017). Exploring gravity wave characteristics in 3-D using a novel S-transform technique: AIRS/Aqua measurements over the southern Andes and Drake passage. *Atmospheric Chemistry and Physics*, *17*(13), 8553–8575. https://doi.org/10.5194/acp-17-8553-2017

Yue, J., Miller, S. D., Hoffmann, L., & Straka, W. C., III. (2014). Stratospheric and mesospheric concentric gravity waves over tropical cyclone Mahasen: Joint AIRS and VIIRS satellite observations. *Journal of atmospheric and solar-terrestrial physics*, *119*, 83–90. https://doi.org/10.1016/j.jastp.2014.07.003

Yue, J., Miller, S. D., Straka, W. C., III, Noh, Y.-J., Chou, M.-Y., Kahn, R., & Flower, V. (2022). La Soufriere volcanic eruptions launched gravity waves into space. *Geophysical Research Letters*, *49*(8). e2022GL097952. https://doi.org/10.1029/2022gl097952